Strict coupling between CFTR's catalytic cycle and gating of its Cl^- ion pore revealed by distributions of open channel burst durations

Proc Natl Acad Sci USA, 107(3), 1241-1246. 10.1073/pnas.0911061107

László Csanády[1], Paola Vergani[2], and David C. Gadsby[3]

[1]Department of Medical Biochemistry, Semmelweis University, Budapest H-1094, Hungary
[2]Neuroscience, Physiology and Pharmacology, University College London, London WC1E 6BT, UK
[3]Laboratory of Cardiac/Membrane Physiology, Rockefeller University, New York, NY 10065, USA

Classification: BIOLOGICAL SCIENCES – Physiology

Corresponding author:

László Csanády, M.D., Ph.D.
Semmelweis University
Department of Medical Biochemistry
Pf. 262, Budapest, H-1444, Hungary
E-mail: laszlo.csanady@eok.sote.hu
Tel: (+36)-1-459-1500/60048
Fax: (+36)-1-267-0031

Manuscript information: text 39489 chars including spaces; 4 figures, 4 SI figures

Abstract

CFTR, the ABC protein defective in cystic fibrosis, functions as an anion channel. Once phosphorylated by protein kinase A, a CFTR channel is opened and closed by events at its two cytosolic nucleotide binding domains (NBDs). Formation of a head-to-tail NBD1/NBD2 heterodimer, by ATP binding in two interfacial composite sites between conserved Walker A and B motifs of one NBD and the ABC-specific signature sequence of the other, has been proposed to trigger channel opening. ATP hydrolysis at the only catalytically competent interfacial site is suggested to then destabilize the NBD dimer and prompt channel closure. But this gating mechanism, and how tightly CFTR channel opening and closing are coupled to its catalytic cycle, remain controversial. Here we determine the distributions of open burst durations of individual CFTR channels, and use maximum likelihood to evaluate fits to equilibrium and non-equilibrium mechanisms and estimate the rate constants that govern channel closure. We examine partially and fully phosphorylated, wild-type CFTR channels, and two mutant CFTR channels each bearing a deleterious mutation in one or other composite ATP binding site. We show that the wild-type CFTR channel gating cycle is essentially irreversible and tightly coupled to the ATPase cycle, and that this coupling is completely destroyed by the NBD2 Walker-B mutation D1370N but only partially disrupted by the NBD1 Walker-A mutation K464A.

Keywords: non-equilibrium, ATPase cycle, maximum likelihood, Walker motifs, phosphorylation

\body

Introduction

ATP-binding cassette (ABC) proteins bind and hydrolyze ATP usually to power transport of substrates across membranes. Their common architecture comprises two transmembrane domains (TMDs), and two cytoplasmic nucleotide binding domains (NBDs) containing conserved sequences for interacting with ATP. Once ATP binds to the conserved Walker A and B motifs of each NBD they dimerize in head-to-tail fashion, burying two ATP molecules in composite interfacial sites (1, 2). Cyclic formation and disruption of the dimer requires hydrolysis of at least one of the ATPs per cycle (3-6).

The ion channel CFTR contains, in addition to canonical ABC-protein domains (TMD1, NBD1, TMD2, NBD2), a unique regulatory (R) domain (7) with multiple cAMP-dependent protein kinase (PKA) targets that must be phosphorylated for ATP to activate bursts of channel openings (Fig. 3A; reviewed in (8)). But the mechanism of CFTR channel gating remains controversial. Early observations that the gating pattern violates microscopic reversibility suggested that the process underlying bursting operates far from thermodynamic equilibrium (9-11). Building on this, on functional evidence from mutants and nucleotide homologs (12-15), and on structural and biochemical data from prokaryotic NBDs (1-4), a CFTR channel open burst was proposed to be initiated by ATP-mediated formation of a stable NBD1-NBD2 heterodimer, and terminated by dimer dissociation after ATP hydrolysis (16). The ATP hydrolysis was posited to occur at the NBD2 composite site (between NBD2 Walker motifs and NBD1 signature sequence) because the NBD1 composite site in CFTR is catalytically inactive (17, 18). In this model (Scheme 2, Fig. 1A), gating cycles are tightly coupled to ATPase cycles (cf., (9, 11-13)), and most open bursts include two kinetically distinct steps: ATP hydrolysis (step $O_1 \rightarrow O_2$) and NBD dimer dissociation (step $O_2 \rightarrow C_2$).

Energetic coupling of residues across the NBD1-NBD2 interface in CFTR in a gating-state-dependent manner (19) supports this model, and it fits with recent structural models of ABC proteins (reviewed in (20)). But it seems hard to reconcile with the puzzling demonstration that mutation of CFTR's NBD1 Walker-A lysine (K464), in the catalytically incompetent composite site, severely impaired ATPase rate while little altering channel gating at saturating ATP (21). This discrepancy suggested that ATPase and gating cycles are not coupled in CFTR. In apparent corroboration of that

interpretation a reversible, equilibrium, model of ATP-activated CFTR gating, like that for ligand-gated channels, has been promoted (22, 23).

To solve this conundrum we have exploited the ability, unique among ABC proteins, to record conformational transitions of single CFTR channel molecules. Because only transitions coupled to pore opening or closing are directly observed in current records, while other transitions (e.g., between two open states) go undetected, CFTR gating studies usually report mean opening and closing rates, which are compound functions of several transition rates. Additional information, hidden in the *shapes* of the distributions of burst and interburst durations, can be extracted by using maximum likelihood (ML) optimization (24) to fit them with the most appropriate model and so learn the underlying transition rates. Here we adopt this strategy to clarify the transitions that govern closure of CFTR channels, and the influence on them of phosphorylation and of mutations in the two ATP-binding sites. Our analysis reveals that wild-type (WT) CFTR has an essentially irreversible gating cycle tightly coupled to ATP hydrolysis, but that catalytic site mutations can modify the degree of coupling.

Results

CFTR gating is characterized by bursting behavior, due to the presence of two readily distinguishable populations of closed events ((25), Fig. S3A, B). A series of (one or more) openings separated by brief "intraburst" closures of ~10 ms is called an open burst, and bursts are flanked by long "interburst" closures of ~1 s duration. Previous work has established that CFTR phosphorylation by PKA, and ATP binding and hydrolysis, regulate the mean open burst and interburst durations (τ_b and τ_{ib}). But to dig deeper into the underlying mechanisms of channel gating and how it is coupled to CFTR's ATPase cycle we examined the *shapes* of the burst duration distributions.

Peaked burst duration distributions reveal essentially irreversible gating cycle for WT CFTR

A simple, readily reversible, closed-open equilibrium model of CFTR gating ((22, 23); submodel Scheme 1, encircled by the *blue* dashed line in Fig. 1A) predicts a single-exponential distribution of open burst durations, but the irreversible cyclic model ((16); full model Scheme 2 in Fig. 1A) predicts a peaked distribution harboring two components – one with a negative fractional amplitude. This is because the prehydrolytic NBD dimer is very stable (13, 15, 19), and the rate of $O_1 \rightarrow C_1$ (k_{-1}) is thus very slow. Consequently, the majority of bursts include two sequential steps, ATP hydrolysis (step $O_1 \rightarrow O_2$) followed by NBD dimer dissociation (step $O_2 \rightarrow C_2$), and this reduces the incidence of very brief bursts.

To reconstruct the distributions of open burst durations for WT CFTR, we recorded currents from dozens of patches containing a single active channel, collecting 1441 bursts in 2 mM ATP, following PKA removal. The resulting burst duration distribution (Fig. 1B) showed a clear peak, rather than monotonic decay. This paucity of brief bursts was not due to limited time resolution, because we included only events longer than t_{low}=6 ms in our analysis (correspondingly, the lowest bins in Fig. 1 start at 6 ms), whereas the filter dead time was 1.8 ms. Accordingly, when we fitted this distribution, using a maximum likelihood approach, to the single-exponential probability density function (pdf) of Scheme 1 (1 free parameter; *blue dotted* line) or to the peaked pdf of Scheme 2 with rate k_{-1} fixed to zero (2 free parameters; *red solid* line), the latter fit proved significantly ($P=2\cdot10^{-9}$) better, as shown by the corresponding large log-likelihood ratio $\Delta LL=18.01$ (cf., (26)). This finding provides strong support for

a non-equilibrium gating cycle with two sequential open conformations, and so suggests that Scheme 2 with a small rate k_{-1} adequately describes the mechanism underlying open bursts of WT CFTR channels.

Burst duration distribution of non-hydrolytic mutant D1370N further supports irreversible mechanism for WT

As a control, we chose to study the NBD2 Walker-B mutant D1370N, because the analogous mutation completely abolished ATP hydrolysis in other ABC proteins (27-29). The distribution of burst durations of D1370N channels gating in 2 mM ATP (Fig. 1C), reconstructed from 530 bursts, indeed differs qualitatively from that of WT channels (Fig. 1B) in that it decays monotonically. When this distribution was fitted by Scheme 2 with k_{-1} fixed to zero, one of the two resulting components was trivially small, and the fit was no better (ΔLL=0) than that by the equilibrium submodel Scheme 1 (*blue dotted* line). This finding for a mutant expected incapable of ATP hydrolysis (k_1=0) validates our interpretation of the peaked WT CFTR distribution as indicative of a highly non-equilibrium gating cycle.

Interestingly, a combination of two positive-amplitude exponential components slightly improved the fit (ΔLL=3.24; P=0.03; *red solid line*, Fig. 1C; see Supp. Inf. for more fitting results) suggesting a mixture of two types of open bursts for D1370N; the major population, with an average lifetime of ~2 s, seems interspersed with a few brief bursts of ~200 ms duration. The latter minor population might reflect the mechanism by which infrequent brief channel openings are observed in the absence of ATP in this mutant (Fig. S3E, *inset*, asterisks) and even less frequently in WT CFTR (16, 30).

Burst duration distribution of K464A mutant reveals profoundly altered gating mechanism

Although the K464A mutation lowers CFTR ATPase turnover rate ~10 fold (21), τ_b was essentially unaffected by this mutation (Fig. 1D, inset). However, the shape of the distribution of K464A burst durations (Fig. 1D; reconstructed from 2327 events) clearly differed from that of WT CFTR. This distribution decayed monotonically, and a fit by Scheme 2 with k_{-1} fixed to zero (2 free parameters) gave no improvement (ΔLL=0) over a fit by Scheme 1 (1 free parameter; *blue dotted line*), providing no

evidence for obligatory sequential progression through two open states. However, because the K464A mutant does carry out some ATP hydrolysis, albeit slowly (21), we also evaluated a *partially* hydrolytic mechanism by leaving k_{-1} in Scheme 2 as a free parameter. This allows some bursts to terminate through reversal of the opening step (rate k_{-1}) and others through hydrolysis of ATP, and hence through state O_2. With k_{-1} free, Scheme 2 did indeed provide a statistically better fit (P=0.027; ΔLL=3.62), evident in the 0-100 ms range (3 free parameters; *red* line). The rate estimates from this fit suggest that in K464A CFTR the rate of the ATP hydrolysis step (k_1) is slowed by only ~4 fold compared to WT, consistent with the fact that this mutation is not in the composite NBD2 site, where ATP hydrolysis occurs. But this analysis also indicates that the K464A mutation greatly destabilizes the prehydrolytic dimer (k_{-1} is increased).

Macroscopic closing rates of non-hydrolytic mutants provide estimates of the rate of non-hydrolytic closure of WT CFTR

The simplification of making the opening step in Scheme 2 irreversible for fitting the burst distribution of WT CFTR (Fig. 1B, *red line*, k_{-1} was set to zero) rests on experimental evidence that reversal of this step, by dissociation of the prehydrolytic NBD1-NBD2 dimer, is far slower than normal channel closure. For example, mutations of the NBD2 Walker A lysine (K1250) or proposed catalytic carboxylate (E1371), shown to abolish or severely impair ATP hydrolysis in CFTR and other ABC proteins (5, 21, 27), prolong τ_b by several orders of magnitude (9, 11, 16, 19). As a 3-parameter fit of Scheme 2 to the data in Fig. 1B (and also 3B, below) did not provide a reliable estimate of this small rate (see Supp. Inf.), to estimate k_{-1} we measured the macroscopic closing rates of prephosphorylated K1250A, K1250R, and E1371S mutant channels (e.g., Fig. 2A) upon sudden removal of ATP. These rates, obtained as the reciprocals of the time constants of fitted single exponentials (e.g., Fig. 2A, *blue line*), were 0.044±0.004 s^{-1} (n=9) for K1250A (Fig. 2C, *blue bar*), 0.22±0.01 s^{-1} (n=17) for K1250R, and 0.036±0.002 s^{-1} (n=16) for E1371S. Their variation likely reflects different specific effects of the mutations on the stability of the prehydrolytic NBD1-NBD2 dimer. As we cannot be certain which of these mutant channels, when open, most closely resembles the O_1 state of a WT CFTR channel gating in ATP, we tentatively chose the closing rate of K1250R as an estimate of k_{-1} for WT CFTR (see Fig. 4E,

right, blue bar), on the grounds that the lysine-to-arginine mutation at least conserves charge in the vicinity of the ATP bound within the NBD2 composite site.

Insofar as ATP hydrolysis is also absent in D1370N (k_1=0), for this mutant the rate of channel closure from an open burst reflects the rate of dissociation of the prehydrolytic NBD dimer (k_{-1}, Fig. 4E, *right, green bar*). This rate is accelerated ≥5-fold compared to WT (*blue bar*), indicating strong destabilization of the prehydrolytic dimer, which is consistent with the proposed role of the Walker-B aspartate in Mg^{2+} binding (1, 29, 31).

Acceleration of non-hydrolytic channel closure by the K464A mutation supports microscopic burst duration analysis

Assuming k_{-1}=0.22 s^{-1} for WT, the ML fit of Scheme 2 to the K464A burst distribution (Fig. 1D) suggests that rate k_{-1} is increased by ~15 fold in K464A CFTR. This conclusion from the distribution of microscopic burst durations is corroborated by the fact that closure of non-hydrolytic CFTR mutants and of WT channels "locked" in open bursts by non-hydrolyzable ATP analogs or by orthovanadate is greatly accelerated by the K464A mutation (16, 18, 30, 32). For instance, closure of the catalytically incompetent NBD2 Walker-A mutant K1250A is accelerated ~10 fold in the double mutant K464A/K1250A, as reported by the rate of macroscopic current decay upon ATP removal (Fig. 2B; *red line* is a single-exponential fit; Fig. 2C, *red bar*).

Phosphorylation slows both sequential steps involved in open-burst closure in WT CFTR channels

The open probability of WT human CFTR channels in inside-out *Xenopus*-oocyte patches exposed to 300 nM PKA + 2 mM ATP declines by ~3 fold immediately after removal of PKA ((16, 33); Figs. 3A, 4A). This rapid drop, attributed to partial dephosphorylation by membrane-bound phosphatases, is due to ~2 fold shortening of τ_b and nearly 2 fold lengthening of τ_{ib} (Fig. 4B, C; *navy blue* vs. *royal blue bars*, cf., (13, 16, 33)).

To dissect the mechanism by which phosphorylation prolongs τ_b, we collected 1085 bursts from single WT CFTR channels gating in the presence of 2 mM ATP + 300 nM PKA. Just as for partially phosphorylated WT, the burst duration distribution of fully phosphorylated WT CFTR (Fig. 3B) showed

a clear peak, rather than monotonic decay, and was significantly ($P=4\cdot10^{-9}$; $\Delta LL=17.34$) better fitted by Scheme 2 with k_{-1} fixed to zero (2 free parameters; *red line*) than by the equilibrium Scheme 1 (1 free parameter; *blue dotted line*). Thus, gating of fully and of partially phosphorylated CFTR channels obeys a qualitatively similar, irreversible mechanism. A comparison of the maximum likelihood estimates of the rates k_1 and k_2 for the two conditions reveals that full phosphorylation slows both rates by ~2 fold, while their ratio k_2/k_1 remains ~11 (Fig. 4E; k_1, *left*; k_2, *center*; compare *royal blue* and *navy blue bars*). So full phosphorylation slows channel closure from an open burst without altering the fractions of time spent in states O_1 and O_2: regardless of the degree of phosphorylation, ~92% of the burst duration appears to be spent waiting for ATP hydrolysis to happen, while the final ~8% can be attributed to the lifetime of the posthydrolytic NBD1-NBD2 dimer. The rapid partial dephosphorylation of CFTR upon PKA removal (Fig. 3A) precludes the use of macroscopic current relaxations (cf., Fig. 2A) to estimate k_{-1} for fully phosphorylated channels.

Perturbations that profoundly alter the mechanism of gating need not greatly alter the cycle time of CFTR channel bursts

Until now, studies of CFTR gating have focused on extracting open probability and average τ_b and τ_{ib}, which are readily obtained from patches containing either single (34, 35) or multiple (36) channels. Figure 4A-C compares such average parameters for fully (*navy blue*) and partially (*royal blue*) phosphorylated WT, and partially phosphorylated D1370N (*green*) and K464A (*red*) CFTR channels. Consistent with previous reports, for D1370N CFTR channels gating in near-saturating ATP (2 mM, (16)) τ_b is ~4 fold longer than, but τ_{ib} is like, that of WT (Fig. 4B, C, *green bars*, cf., (9, 16, 30), whereas for prephosphorylated K464A CFTR channels in saturating ATP (5 mM, (16)) τ_b is comparable to, but τ_{ib} is at least ~2 fold longer than, that of WT (Fig. 4B, C, *red bars*; (9, 14, 16) but, cf., (32)). However, as the mean length of an entire gating cycle is given by $\tau_b+\tau_{ib}$, the calculated cycle time (Fig. 4D) is only modestly changed by the presence of PKA or by either mutation. In contrast, the rate estimates from our present analysis (Fig. 4E, k_1, *left*; k_2, *center*; k_{-1}, *right*) reveal that the same perturbations profoundly alter the microscopic transition rates that determine the mechanism by which bursts are terminated.

Discussion

Maximum likelihood fitting allows quantitative comparison of alternative gating mechanisms, since the log-likelihood ratio for a pair of models provides a measure of their relative applicability, expressible in terms of statistical significance (24, 26). We used this strategy to see whether the distributions of CFTR open burst durations are more consistent with a reversible, equilibrium, gating mechanism or with an irreversible, non-equilibrium, one. The large improvements we found in the fits for WT CFTR (Figs. 1B, 3B) by using a cyclic scheme (Scheme 2) as opposed to a closed-open model (Scheme 1) strongly support an irreversible mechanism. The interpretation that this irreversible cycle is driven by ATP hydrolysis is validated by the lack of any such fit improvement for the presumed non-hydrolytic D1370N mutant (Fig. 1C). As a bonus, the fits give first estimates for the rates of the two consecutive steps that govern WT CFTR channel closure (Fig. 4E).

Because the pdf for Scheme 2 with k_{-1}=0 (see Methods) is symmetrical with respect to rates k_1 and k_2, the fits to the WT burst duration distributions cannot specify whether k_1 is slow and k_2 fast, or vice versa. We assigned k_1 as the slow rate and k_2 as the fast rate for WT CFTR channels (Fig. 4E, *left* and *center*) on the basis of much previous work that suggests that ATP hydrolysis rate limits closure from an open burst (e.g., (9, 13-15)). However, the fit for K464A provides additional support for this assignment. For k_{-1}>0 the burst-pdf for Scheme 2 (Methods) is no longer symmetrical with respect to k_1 and k_2, and it can be shown that for any set of rates k_1, k_2, k_{-1}, for which k_2>k_{-1} holds, there exists a single alternative set k_1', k_2', k_{-1}' (given by k_1'=k_2-k_{-1}, k_2'=k_1+k_{-1}, k_{-1}'=k_{-1}) which yields an identical pdf. Thus, the set k_1'=15.4 s^{-1}, k_2'=4.30 s^{-1}, k_{-1}'=3.39 s^{-1} fits the observed pdf for K464A just as well as the set displayed in Fig. 4E (k_1=0.91 s^{-1}, k_2=18.8 s^{-1}, k_{-1}=3.39 s^{-1}). But this alternative set can be ruled out as it would yield an essentially hydrolytic mechanism for K464A (with a coupling ratio of ~82%) in contradiction of the observed severe defect in ATPase turnover rate (21). Together, these data validate our premise of a slow step $O_1 \rightarrow O_2$ followed by a faster step $O_2 \rightarrow C_2$.

The NBD1 Walker-A mutant K464A has received much previous attention. That this mutation, in a catalytically inactive binding site (17, 18), affects channel gating only slightly (Fig. 4D; cf., (16, 21, 32)) contrasts with its substantial suppression of the rate of ATP hydrolysis of purified K464A CFTR protein (to <10% of WT; (21)). The altered shape of the distribution of K464A burst durations (Fig. 1D)

now provides a satisfying explanation for this dissociation between channel cycle time and ATPase rate. The ratio $k_1/(k_1+k_{-1})$ estimated from the Scheme-2 fit (*red bars*, Fig.4E, *left* and *right*) suggests that in K464A only ~1 out of every 5 bursts proceeds through the normal irreversible hydrolytic pathway (Fig. 4F). This "coupling ratio" between channel opening and ATP hydrolysis of ~21% for K464A CFTR contrasts with that of ≥95% for WT channels (*blue bars*, Fig. 4E, *left* and *right*; Fig. 4F). Because the cycle time of K464A channels is prolonged ~2 fold compared to WT (Fig. 4D), the predicted overall ATPase turnover rate is on the order of 10% of WT, which is in very reasonable agreement with the measured value (21). The non-hydrolytic NBD2 mutant D1370N is a more extreme case, with an estimated coupling ratio of 0% (*green bars*, Fig. 4E, *left* and *right*; Fig. 4F).

The mechanism by which strong phosphorylation by PKA prolongs τ_b (13, 16, 33) has remained a puzzle. We show here that PKA slows closure by decreasing both rates k_1 and k_2 (Fig. 4E), without altering their ratio, and this can explain two poorly understood facts. First, the similar activation enthalpies for closure of partially and fully phosphorylated CFTR suggested that both are rate limited by the same step (37), and we can now identify this step as ATP hydrolysis (k_1). Second, exposing CFTR channels to ATP plus orthovanadate results in long "locked-open" bursts (12, 15), and the rate at which *open* channels become locked by orthovanadate was found not to depend on τ_b (12). Because orthovanadate must bind to, and stabilize, the posthydrolytic dimer (O_2) this rate of locking reflects the fraction of the open burst time spent in O_2 – which we now show to be independent of τ_b.

In a working transporter the substrate-binding site is exposed alternately to the two sides of the membrane. For ABC exporters, formation of the tight NBD dimer is believed (20) to flip the transmembrane domains from an inward- to an outward-facing conformation. In CFTR, formation of the NBD dimer opens the channel (16, 19), suggesting that CFTR can be viewed as a "degraded" ABC exporter in which the ATP-bound conformation with outward-facing TMDs somehow allows downhill flow of Cl^- ions through a transmembrane pore (Fig. 4F, *right*). However, we show here that certain severe mutilations of CFTR's catalytic cycle can leave the superficial gating parameters (τ_b and τ_{ib}; Fig. 4B-D) and hence the net rate of Cl^- transport not greatly altered. Our analysis of the D1370N mutant, for example, implies that this mutation does not prevent cycling between inward- (closed channel) and outward-facing (open channel) conformations of CFTR (Fig. 4D, *green*; cf., Fig. 4F). If the D-to-N

mutation of the Walker-B aspartate were to similarly preserve inward-outward conformation flips in ABC exporters, then why would it abolish their active transport, as observed (27, 28)? To transport substrate uphill, the energy of ATP hydrolysis must be harnessed to convert the substrate binding sites in the transmembrane domain from a high affinity to the low-affinity conformation needed to ensure substrate release at the higher-concentration side. It seems reasonable to propose that in an ABC exporter this affinity switch does not coincide with the transition to the outward-facing conformation. In other words, partial cycles reversing from the state corresponding to O_1 do not result in net substrate extrusion. Instead, in ABC exporters the high-to-low affinity conversion of the substrate-binding site is likely linked to the ATP hydrolysis step itself (cf., transition $O_1 \rightarrow O_2$). This would explain why catalytic-site mutations in such transporters result in parallel disruption of transport and ATPase turnover rates (27, 28). Intriguingly, in CFTR, a vestige of this affinity-switch conformational change (cartooned as a change in TMD shape between states O_1 and O_2 in Fig. 4F) can be observed, under appropriate conditions, as a subtle change in permeation properties of the CFTR channel pore (9, 10).

Our results highlight the superior discriminative power afforded by analyzing the distributions of CFTR burst durations rather than just their mean values, and exploit the unprecedented opportunity this approach offers to characterize the steps underlying termination of open-channel bursts in an ABC transporter broken by evolution.

Methods

Molecular biology

Mutations were introduced into pGEMHE-CFTR using QuikChange (Stratagene) as previously described (16); cDNA was transcribed in vitro with T7 polymerase (Ambion) and cRNA stored at -80^{o}C.

Isolation and injection of Xenopus oocytes

Oocytes were isolated from anaesthethized adult female *Xenopus* laevis and injected with cRNA as described (33). Single-channel and macroscopic recordings were made 2-3 days after injection of 0.03-10 ng of cRNA.

Excised inside-out patch recording

Patch pipette solution contained (in mM): 136 NMDG-Cl, 2 $MgCl_2$, 5 HEPES, pH=7.4 with NMDG. Bath solution contained (in mM): 134 NMDG-Cl, 2 $MgCl_2$, 5 HEPES, 0.5 EGTA, pH=7.1 with NMDG. 2-5 mM MgATP was added from a 400-mM aqueous stock solution (pH=7.1 with NMDG). 300 nM catalytic subunit of PKA (Sigma) was used to activate CFTR channels. Currents were recorded at a pipette holding potential of +80 mV (V_m=-80 mV), digitized at 10 kHz, and recorded to disk after on-line Gaussian filtering at 1 kHz.

Kinetic analysis of multichannel records

Records with 1-8 channels were analyzed as described (33). Currents were digitally filtered at 100 Hz, and idealized by half-amplitude threshold crossing. Events lists were fitted with a simple model in which ATP-dependent slow gating is pooled into a closed-open scheme and brief closures modeled as pore-blockage events (10). Rate constants (r_{CO}, r_{OC}, r_{OB}, r_{BO}) of the resulting Closed-Open-Blocked (C↔O↔B) scheme were extracted by a simultaneous ML fit to the dwell-time histograms of all conductance levels, while accounting for the filter dead time (36). τ_{ib} and τ_b (Fig. 4B,C) were then calculated as $\tau_{ib}=1/r_{CO}$, and $\tau_b=(1/r_{OC})(1+ r_{OB}/r_{BO})$.

Burst analysis of single-channel records

Individual components of the closed-time distribution were assigned as intra- or interburst based on their ATP-dependence (see Supp. Inf., Fig. S3). Open bursts were isolated by ignoring closures shorter than a cutoff (t_{crit}). Two strategies for choosing t_{crit} are described in (34) (method (i)) and (35) (method (ii)). We employed large simulated data sets to study the distortion of the distribution of bursts resulting from these two procedures. Method (ii) proved slightly more accurate for estimating the mean of a single-exponential burst distribution (Fig. S1), but measurably distorted the shape, and the resulting rate estimates, for the peaked distribution characteristic of a cyclic mechanism (Fig. S2). Therefore, although both methods yielded qualitatively similar results, we used the distributions obtained using method (i) for WT and K464A (Figs. 1B, 1D, 3B; Fig. 4) but that obtained using method (ii) for D1370N (Fig. 1C).

The distributions of the durations of bursts obtained in this way were fitted to various models using ML (24), by excluding events shorter than t_{low}=6 ms. The burst pdf for Scheme 1 is given by $f(t)=k*\exp(-kt)$, that for Scheme 2 with $k_{-1}=0$ by $f(t)=(k_1k_2/(k_1-k_2))*(\exp(-k_1t)-\exp(-k_2t))$, and that for the full Scheme 2 by $f(t)=((k_{-1}-k_2)(k_{-1}+k_1)/(k_{-1}+k_1-k_2))*\exp(-(k_{-1}+k_1)t) + (k_1k_2/(k_{-1}+k_1-k_2))*\exp(-k_2t)$. The improvement of a fit due to introduction of an additional parameter was evaluated using the log-likelihood ratio test (26); a more comprehensive summary of ML fitting results is given in Supp. Inf. (Fig. S4).

Fitting of macroscopic current relaxations

Macroscopic current decay time courses were fit by single-exponential functions using non-linear least-squares methods (pCLAMP 9, Axon Instruments, Inc.).

Acknowledgements

We thank Dorottya Mayer for oocyte isolation and injection. Supported by NIH grant R01-DK051767, NIH Fogarty International Center grant R03-TW007829, and Wellcome Trust grant 081298/Z/06/Z.

Figure legends

Figure 1. Distributions of burst durations for WT and mutant CFTR channels. *A*, Non-equilibrium cyclic full model (Scheme 2) proposed to describe CFTR gating. The equilibrium closed-open model (Scheme 1, encircled by *blue* dotted line), is a submodel of Scheme 2. *B-D*, Histograms of open burst durations for pre-phosphorylated WT (*B*), D1370N (*C*) and K464A (*D*) CFTR channels; 30-s segments of representative single-channel current recordings are shown above each panel. The lowest bins start at t_{low}=6 ms. *Blue dotted lines* show ML fits to Scheme 1. *Red solid lines* in panels *B* and *D* show ML fits to Scheme 2; rate k_{-1} was fixed to zero in *B*, but left free in *D*. In panel C *red solid line* shows the ML fit to a double-exponential distribution. Obtained rate estimates, as well as time constants and fractional amplitudes of the resulting exponential components, are printed in *red*. [ATP] was 2 mM for WT and D1370N, but 5 mM for K464A.

Figure 2. Slow non-hydrolytic closing rate, and its acceleration by the K464A mutation. *A*, *B*, Macroscopic currents of prephosphorylated K1250A (*A*) and K464A/K1250A (*B*) CFTR channels were activated by application of 10 mM ATP. Time courses of current decay upon ATP removal were fitted by single exponentials (*colored lines*). *C*, Mean (± S.E.M.) closing rates, estimated as the inverses of the current relaxation time constants (τ_{relax}), for K1250A (*blue*) and K464A/K1250A (*red*).

Figure 3. Phosphorylation slows both sequential steps involved in CFTR channel closure. *A*, Channel activity of WT CFTR rapidly declines upon PKA removal, but then remains steady for a prolonged period of time, thereby defining gating patterns for "fully" (in the presence of PKA) and "partially" phosphorylated CFTR (in just ATP, following PKA withdrawal). *B*, Histogram of open burst durations for fully phosphorylated WT CFTR channels; and 30-s segment of single-channel current recording. Lowest bin starts at t_{low}=6 ms. *Blue dotted line* is a ML fit to Scheme 1. *Red solid line* is a ML fit to Scheme 2 with rate k_{-1} fixed to zero.

Figure 4. Average gating parameters, gating mechanisms, and microscopic transition rate estimates for WT and mutant CFTR channels. *A-D*, Open probabilities (*A*), mean burst (*B*) and

interburst (*C*) durations obtained from multi-channel fits, and calculated channel cycle times (*D*), for fully (*navy blue*) and partially phosphorylated WT (*royal blue*), and partially phosphorylated D1370N (*green*) and K464A (*red*) CFTR. [ATP] was 2 mM for WT and D1370N, but 5 mM for K464A. Error bars represent S.E.M. *E*, ML estimates of rates k_1 (*left*), k_2 (*center*), and k_{-1} (*right*) for fully (*navy blue*) and partially phosphorylated WT (*royal blue*), and partially phosphorylated D1370N (*green*) and K464A (*red*) CFTR channels. Error bars represent 0.5-unit log-likelihood intervals. [(a)] k_{-1} for partially phosphorylated WT is modeled by the closing rate of partially phosphorylated K1250R. *F*, Cartoon of gating mechanisms. NBD1, *green*; NBD2, *blue*; TMDs, *cyan*; ATP, *yellow*; ADP, *red*. Probabilities for exiting state O_1 (*top right state*) in either of two possible directions are printed in color for partially phosphorylated WT (*blue*), K464A (*red*), and D1370N (*green*). Note subtle shape change in TMDs between O_1 and O_2 (see text).

References

1. Hopfner, K. P., Karcher, A., Shin, D. S., Craig, L., Arthur, L. M., Carney, J. P. & Tainer, J. A. (2000) Structural biology of Rad50 ATPase: ATP-driven conformational control in DNA double-strand break repair and the ABC-ATPase superfamily *Cell* **101**, 789-800.

2. Smith, P. C., Karpowich, N., Millen, L., Moody, J. E., Rosen, J., Thomas, P. J. & Hunt, J. F. (2002) ATP binding to the motor domain from an ABC transporter drives formation of a nucleotide sandwich dimer *Mol. Cell* **10**, 139-149.

3. Verdon, G., Albers, S. V., van Oosterwijk, N., Dijkstra, B. W., Driessen, A. J. & Thunnissen, A. M. (2003) Formation of the productive ATP-Mg2+-bound dimer of GlcV, an ABC-ATPase from Sulfolobus solfataricus *J. Mol. Biol.* **334**, 255-267.

4. Moody, J. E., Millen, L., Binns, D., Hunt, J. F. & Thomas, P. J. (2002) Cooperative, ATP-dependent association of the nucleotide binding cassettes during the catalytic cycle of ATP-binding cassette transporters *J. Biol. Chem.* **277**, 21111-21114.

5. Janas, E., Hofacker, M., Chen, M., Gompf, S., van der, D. C. & Tampe, R. (2003) The ATP hydrolysis cycle of the nucleotide-binding domain of the mitochondrial ATP-binding cassette transporter Mdl1p *J. Biol. Chem.* **278**, 26862-26869.

6. Tombline, G. & Senior, A. E. (2005) The occluded nucleotide conformation of p-glycoprotein *J. Bioenerg. Biomembr.* **37**, 497-500.

7. Riordan, J. R., Rommens, J. M., Kerem, B., Alon, N., Rozmahel, R., Grzelczak, Z., Zielenski, J., Lok, S., Plavsic, N., Chou, J. L. *et al.* (1989) Identification of the cystic fibrosis gene: cloning and characterization of complementary DNA *Science* **245**, 1066-1073.

8. Chen, T. Y. & Hwang, T. C. (2008) CLC-0 and CFTR: chloride channels evolved from transporters *Physiol Rev.* **88**, 351-387.

9. Gunderson, K. L. & Kopito, R. R. (1995) Conformational states of CFTR associated with channel gating: the role ATP binding and hydrolysis *Cell* **82**, 231-239.

10. Ishihara, H. & Welsh, M. J. (1997) Block by MOPS reveals a conformation change in the CFTR pore produced by ATP hydrolysis *Am. J. Physiol* **273**, C1278-C1289.

11. Zeltwanger, S., Wang, F., Wang, G. T., Gillis, K. D. & Hwang, T. C. (1999) Gating of cystic fibrosis transmembrane conductance regulator chloride channels by adenosine triphosphate hydrolysis. Quantitative analysis of a cyclic gating scheme *J. Gen. Physiol* **113**, 541-554.

12. Baukrowitz, T., Hwang, T. C., Nairn, A. C. & Gadsby, D. C. (1994) Coupling of CFTR Cl- channel gating to an ATP hydrolysis cycle *Neuron* **12**, 473-482.

13. Hwang, T. C., Nagel, G., Nairn, A. C. & Gadsby, D. C. (1994) Regulation of the gating of cystic fibrosis transmembrane conductance regulator C1 channels by phosphorylation and ATP hydrolysis *Proc. Natl. Acad. Sci. U. S. A* **91**, 4698-4702.

14. Carson, M. R., Travis, S. M. & Welsh, M. J. (1995) The two nucleotide-binding domains of cystic fibrosis transmembrane conductance regulator (CFTR) have distinct functions in controlling channel activity *J. Biol. Chem.* **270**, 1711-1717.

15. Gunderson, K. L. & Kopito, R. R. (1994) Effects of pyrophosphate and nucleotide analogs suggest a role for ATP hydrolysis in cystic fibrosis transmembrane regulator channel gating *J. Biol. Chem.* **269**, 19349-19353.

16. Vergani, P., Nairn, A. C. & Gadsby, D. C. (2003) On the mechanism of MgATP-dependent gating of CFTR Cl- channels *J. Gen. Physiol* **121**, 17-36.

17. Aleksandrov, L., Aleksandrov, A. A., Chang, X. B. & Riordan, J. R. (2002) The First Nucleotide Binding Domain of Cystic Fibrosis Transmembrane Conductance Regulator Is a Site of Stable Nucleotide Interaction, whereas the Second Is a Site of Rapid Turnover *J. Biol. Chem.* **277**, 15419-15425.

18. Basso, C., Vergani, P., Nairn, A. C. & Gadsby, D. C. (2003) Prolonged nonhydrolytic interaction of nucleotide with CFTR's NH2-terminal nucleotide binding domain and its role in channel gating *J. Gen. Physiol* **122**, 333-348.

19. Vergani, P., Lockless, S. W., Nairn, A. C. & Gadsby, D. C. (2005) CFTR channel opening by ATP-driven tight dimerization of its nucleotide-binding domains *Nature* **433**, 876-880.

20. Hollenstein, K., Dawson, R. J. & Locher, K. P. (2007) Structure and mechanism of ABC transporter proteins *Curr. Opin. Struct. Biol.* **17**, 412-418.

21. Ramjeesingh, M., Li, C., Garami, E., Huan, L. J., Galley, K., Wang, Y. & Bear, C. E. (1999) Walker mutations reveal loose relationship between catalytic and channel-gating activities of purified CFTR (cystic fibrosis transmembrane conductance regulator) *Biochemistry* **38**, 1463-1468.

22. Aleksandrov, A. A. & Riordan, J. R. (1998) Regulation of CFTR ion channel gating by MgATP *FEBS Lett.* **431**, 97-101.

23. Aleksandrov, A. A., Cui, L. & Riordan, J. R. (2009) Relationship between nucleotide binding and ion channel gating in cystic fibrosis transmembrane conductance regulator *J. Physiol* **587**, 2875-2886.

24. Colquhoun, D. & Sigworth, F. J. (1995) in *Single channel recording*, eds. Sakmann, B. & Neher, E. (*Plenum Press*, New York).

25. Winter, M. C., Sheppard, D. N., Carson, M. R. & Welsh, M. J. (1994) Effect of ATP concentration on CFTR Cl- channels: a kinetic analysis of channel regulation *Biophys. J.* **66**, 1398-1403.

26. Csanády, L. (2006) Statistical evaluation of ion-channel gating models based on distributions of LogLikelihood Ratios *Biophys. J.* **90**, 3523-3545.

27. Urbatsch, I. L., Beaudet, L., Carrier, I. & Gros, P. (1998) Mutations in either nucleotide-binding site of P-glycoprotein (Mdr3) prevent vanadate trapping of nucleotide at both sites *Biochemistry* **37**, 4592-4602.

28. Hrycyna, C. A., Ramachandra, M., Germann, U. A., Cheng, P. W., Pastan, I. & Gottesman, M. M. (1999) Both ATP sites of human P-glycoprotein are essential but not symmetric *Biochemistry* **38**, 13887-13899.

29. Rai, V., Gaur, M., Shukla, S., Shukla, S., Ambudkar, S. V., Komath, S. S. & Prasad, R. (2006) Conserved Asp327 of walker B motif in the N-terminal nucleotide binding domain (NBD-1) of Cdr1p of Candida albicans has acquired a new role in ATP hydrolysis *Biochemistry* **45**, 14726-14739.

30. Bompadre, S. G., Cho, J. H., Wang, X., Zou, X., Sohma, Y., Li, M. & Hwang, T. C. (2005) CFTR gating II: Effects of nucleotide binding on the stability of open states *J. Gen. Physiol* **125**, 377-394.

31. Hung, L. W., Wang, I. X., Nikaido, K., Liu, P. Q., Ames, G. F. & Kim, S. H. (1998) Crystal structure of the ATP-binding subunit of an ABC transporter *Nature* **396**, 703-707.

32. Powe, A. C., Jr., Al Nakkash, L., Li, M. & Hwang, T. C. (2002) Mutation of Walker-A lysine 464 in cystic fibrosis transmembrane conductance regulator reveals functional interaction between its nucleotide-binding domains *J. Physiol* **539**, 333-346.

33. Csanády, L., Chan, K. W., Seto-Young, D., Kopsco, D. C., Nairn, A. C. & Gadsby, D. C. (2000) Severed channels probe regulation of gating of cystic fibrosis transmembrane conductance regulator by its cytoplasmic domains *J. Gen. Physiol* **116**, 477-500.

34. Jackson, M. B., Wong, B. S., Morris, C. E., Lecar, H. & Christian, C. N. (1983) Successive openings of the same acetylcholine receptor channel are correlated in open time *Biophys. J.* **42**, 109-114.

35. Magleby, K. L. & Pallotta, B. S. (1983) Burst kinetics of single calcium-activated potassium channels in cultured rat muscle *J. Physiol* **344**, 605-623.

36. Csanády, L. (2000) Rapid kinetic analysis of multichannel records by a simultaneous fit to all dwell-time histograms *Biophys. J.* **78**, 785-799.

37. Csanády, L., Nairn, A. C. & Gadsby, D. C. (2006) Thermodynamics of CFTR channel gating: a spreading conformational change initiates an irreversible gating cycle *J. Gen. Physiol* **128**, 523-533.

Fig. 1

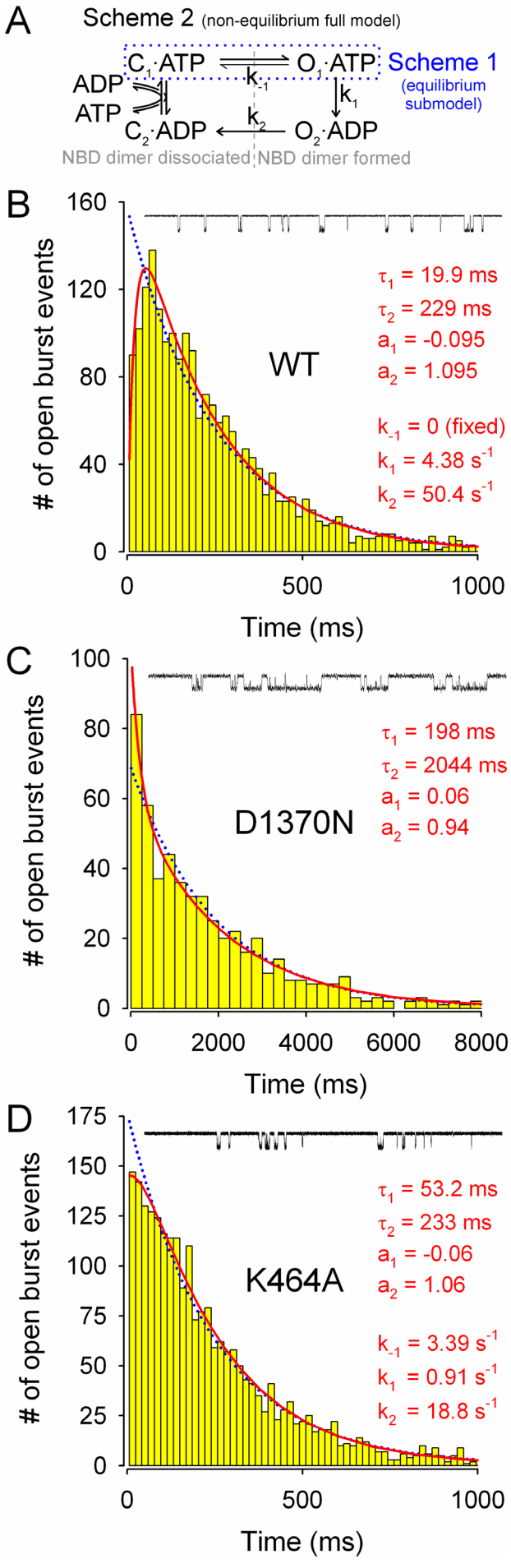
A
Scheme 2 (non-equilibrium full model)
C1·ATP
O1·ATP
Scheme 1
(equilibrium submodel)
ADP
ATP
k-1
k1
k2
C2·ADP
O2·ADP
NBD dimer dissociated
NBD dimer formed
B
# of open burst events
Time (ms)
τ1 = 19.9 ms
τ2 = 229 ms
a1 = -0.095
a2 = 1.095
WT
k-1 = 0 (fixed)
k1 = 4.38 s-1
k2 = 50.4 s-1
C
# of open burst events
Time (ms)
τ1 = 198 ms
τ2 = 2044 ms
a1 = 0.06
a2 = 0.94
D1370N
D
# of open burst events
Time (ms)
τ1 = 53.2 ms
τ2 = 233 ms
a1 = -0.06
a2 = 1.06
K464A
k-1 = 3.39 s-1
k1 = 0.91 s-1
k2 = 18.8 s-1

Fig. 2

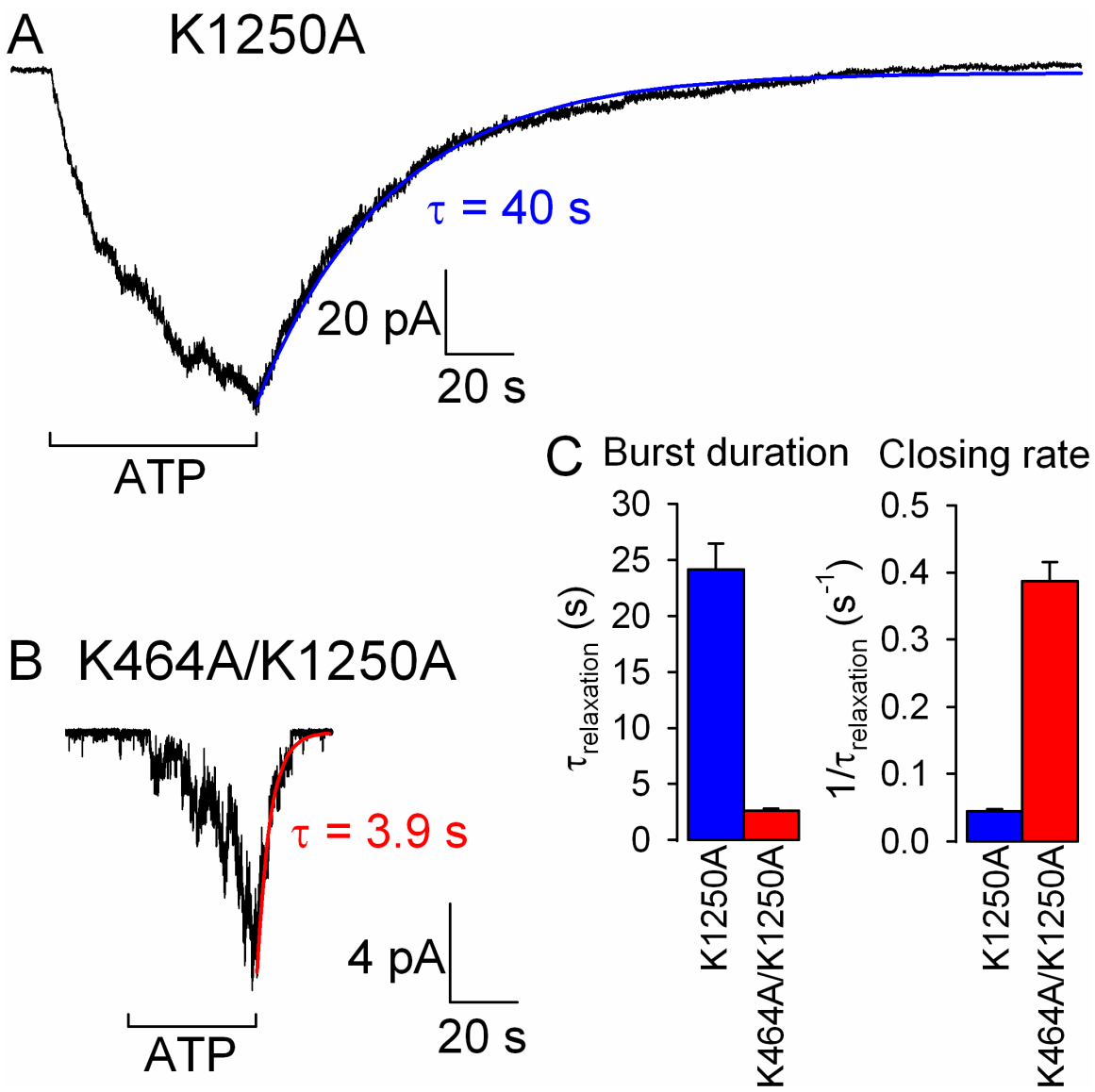
A
K1250A
τ = 40 s
20 pA
20 s
ATP
B
K464A/K1250A
τ = 3.9 s
4 pA
20 s
ATP
C
Burst duration
Closing rate
τrelaxation (s)
1/τrelaxation (s-1)
30
25
20
15
10
5
0
0.5
0.4
0.3
0.2
0.1
0.0
K1250A
K464A/K1250A
K1250A
K464A/K1250A

Fig. 3

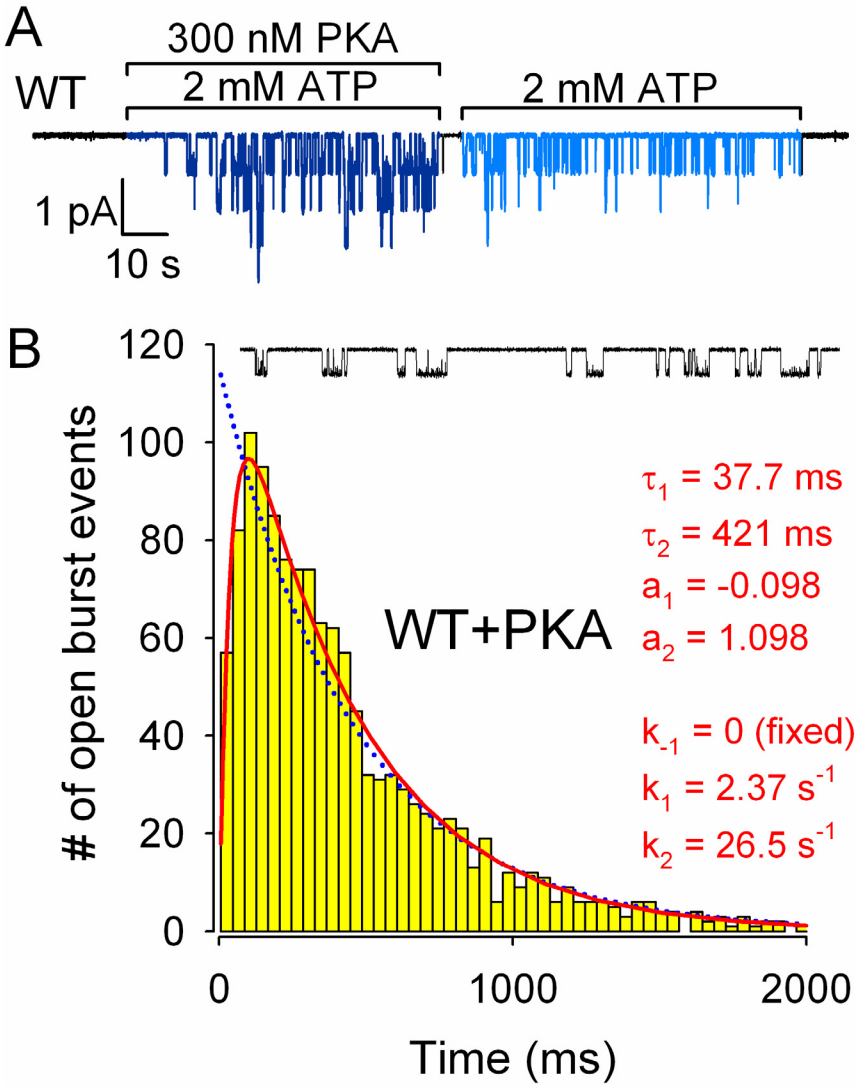
A
300 nM PKA
2 mM ATP
2 mM ATP
WT
1 pA
10 s
B
120
100
80
60
40
20
0
# of open burst events
WT+PKA
τ1 = 37.7 ms
τ2 = 421 ms
a1 = -0.098
a2 = 1.098
k-1 = 0 (fixed)
k1 = 2.37 s-1
k2 = 26.5 s-1
0
1000
2000
Time (ms)

Fig. 4

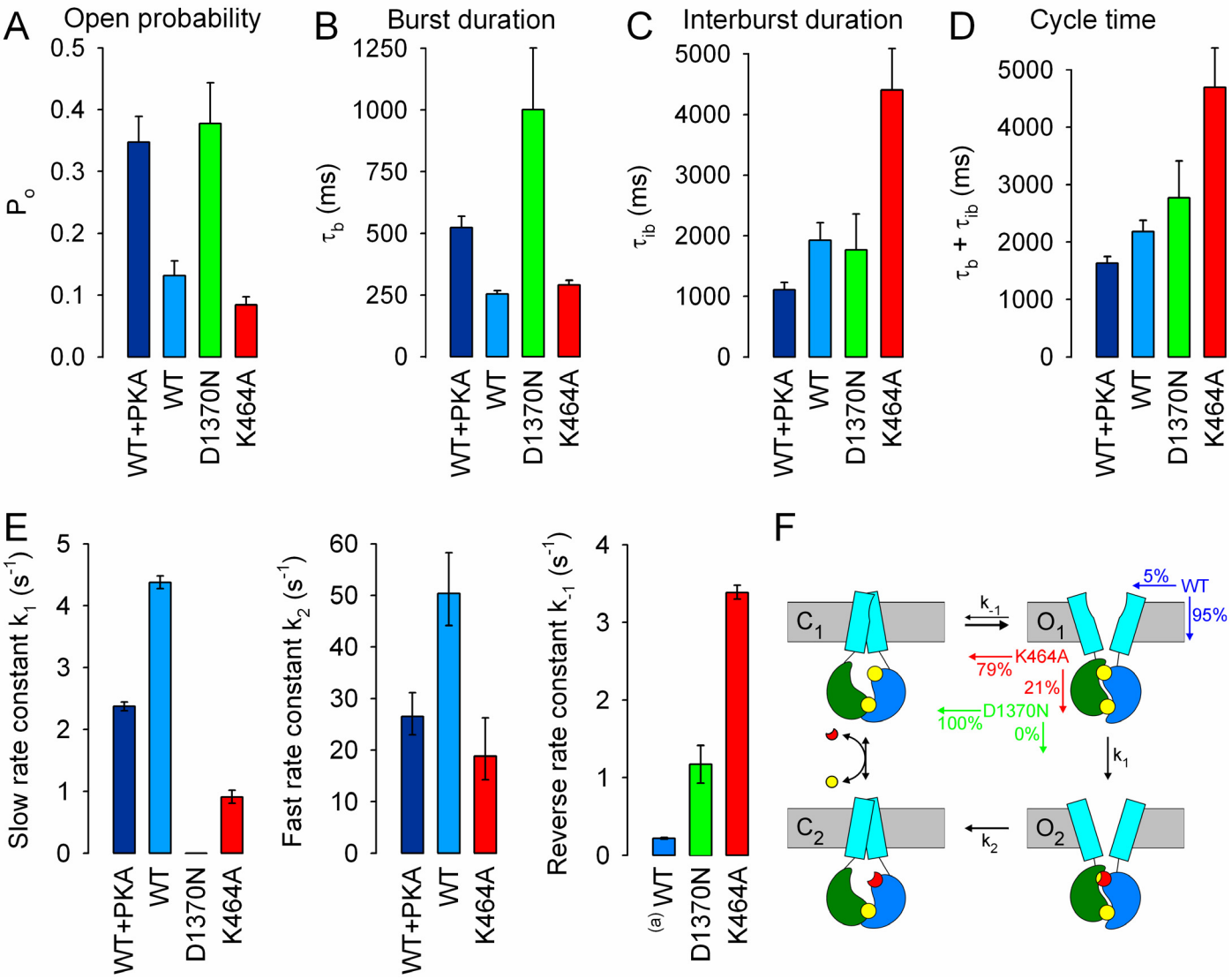
A
Open probability
P_o
0.5
0.4
0.3
0.2
0.1
0.0
WT+PKA
WT
D1370N
K464A
B
Burst duration
τ_b (ms)
1250
1000
750
500
250
0
C
Interburst duration
τ_{ib} (ms)
5000
4000
3000
2000
1000
0
D
Cycle time
$\tau_b + \tau_{ib}$ (ms)
E
Slow rate constant k_1 (s^{-1})
Fast rate constant k_2 (s^{-1})
Reverse rate constant k_{-1} (s^{-1})
(a)
F
C_1
O_1
C_2
O_2
k_{-1}
k_1
k_2
5%
WT
95%
K464A
79%
21%
D1370N
100%
0%

Supporting Information

for

Strict coupling between CFTR's catalytic cycle and gating of its Cl^- ion pore revealed by distributions of open channel burst durations

László Csanády[1], Paola Vergani[2], and David C. Gadsby[3]

[1]Department of Medical Biochemistry, Semmelweis University, Budapest H-1094, Hungary
[2]Neuroscience, Physiology and Pharmacology, University College London, London WC1E 6BT, UK
[3]Laboratory of Cardiac/Membrane Physiology, Rockefeller University, New York, NY 10065, USA

Classification: BIOLOGICAL SCIENCES – Physiology

Corresponding author:

László Csanády, M.D., Ph.D.
Semmelweis University
Department of Medical Biochemistry
Pf. 262, Budapest, H-1444, Hungary
E-mail: laszlo.csanady@eok.sote.hu
Tel: (+36)-1-459-1500/60048
Fax: (+36)-1-267-0031

Comparing strategies for choosing t_{crit} for burst analysis

Because the durations of intra- and interburst closures overlap, the true sequence of open bursts cannot be flawlessly reconstructed; regardless of the choice of t_{crit} there will be a fraction of interburst closures shorter than t_{crit} (these will be erroneously discarded) and a fraction of intraburst closures longer than t_{crit} (these will be retained and mistakenly treated as interburst closures). Two strategies for choosing t_{crit} are (i) to minimize the total number of misclassified closures (34), or (ii) to equalize the numbers of misclassified intra- and interburst closures (35). Because the inevitable distortion of the true burst distributions by these two (and other) procedures have not yet been studied, we used large simulated data sets to evaluate this distortion for methods (i) and (ii), when applied to a single-exponential burst distribution (Fig. S1) and to a peaked burst distribution resulting from a non-equilibrium mechanism (Fig. S2). As expected, our analysis found method (i) slightly more accurate for extracting the average length of single-exponentially distributed bursts (Fig. S1). However, we found that method (ii) caused less overall distortion of burst distributions, and consequently produced more accurate rate estimates for an irreversible cyclic mechanism similar to Scheme 2 of this paper (Fig. S2). It must be noted that the relative accuracy of the two methods in preserving the shapes of burst duration distributions is likely to depend on the particular models and the values of their rate constants. It is therefore recommended that an evaluation similar to that described here be undertaken for each case.

Defining the durations of ATP-driven open bursts for WT and mutant CFTR channels

Opening of CFTR channels from an interburst closure requires binding of ATP, as reflected by the [ATP] dependence of the mean interburst (but not intraburst) duration (τ_{ib}) (25, 16). In contrast, the lack of [ATP] dependence of the microscopic mean open burst duration (τ_b) shows that, once open, a CFTR channel can proceed through a burst of openings without further ATP binding (25, 16, 33). Consequently, the time constant of macroscopic current decay after sudden ATP removal from inside-out patches containing many CFTR channels is identical to the microscopic τ_b ((33, 30), Fig. S3A), so providing an alternative way to estimate burst length.

In this work we also examine the gating behavior of NBD1 Walker A mutant CFTR, K464A, and of NBD2 Walker B mutant CFTR, D1370N. As the pattern of steady-state gating may be more complex in catalytic site mutants (e.g., (30)), two types of information can aid assignment of a particular closed-time component as intra- or interburst. First, the predicted microscopic τ_b should match the time constant of macroscopic current decay upon ATP withdrawal, as just described. Second, in such ATP-removal experiments, closed events can be collected from the periods of time during which only a single CFTR channel is left in the open bursting state before it too finally closes for good. The distribution of such closures – which must all be intraburst given the absence of ATP – can be compared to the closed-time distribution obtained from steady-state gating in ATP (30). For instance, D1370N CFTR (Fig. S3C) has a closed-time distribution in ATP with four discernible exponential components (Fig. S3D), the shortest two of which we could confidently assign as intraburst, because (i) the time constant of macroscopic current decay following removal of ATP from patches containing many D1370N channels (Fig. S3E) matches the steady-state burst duration calculated assuming 2 intra- and 2 interburst components (Fig. S3D), and (ii) the closed-time distribution of the last open channel following removal of ATP (Fig. S3E, blue bar) contains two components (Fig. S3F) with time constants identical to those of the two briefest components of the steady-state closed-time distribution (Fig. S3D).

Systematic ML evaluation of a full range of models for each set of data

ML fitting allows quantitative comparison of alternative gating models because it provides a numerical value for the "goodness" of a fit in the form of the log-likelihood score (LL). When comparing two models with equal numbers of free parameters, the model which provides a higher LL value is ranked higher. Comparing models with different numbers of free parameters is more problematic, because more free parameters always results in a higher LL value, even if introduction of the additional parameters is not justified. However, if the model with fewer parameters is a submodel of the other (the models are nested) and certain regularity criteria apply, the distribution of expected log-likelihood ratios ($\Delta LL=LL_2-LL_1$) can be calculated and compared with the observed value of ΔLL (ΔLL_{obs}). In such cases the two models can be ranked using the log-likelihood ratio test. Thus, for a

given significance level P (e.g., 0.05, 0.01, etc.) the larger model is ranked higher if $\int_{\Delta LL_{obs}}^{\infty} h(x)dx < P$ holds ($h(x)$ is the expected pdf of ΔLL values) – otherwise the submodel is ranked higher.

Using this methodology, we systematically ranked two linear and four cyclic models (Fig. S4A; free parameters are depicted in *red*) for their ability to account for the four datasets described in this paper, i.e., the distributions of burst durations of fully phosphorylated WT, and partially phosphorylated WT, K464A, and D1370N CFTR channels. Schemes 1 and 2 are identical to those shown in Fig. 1A except that, for purposes of studying open bursts, the two closed states C_1 and C_2 in Fig. 1A are merged here into compound state C. In Schemes 2a and 2b rate k_{-1} is fixed either to zero (cf., Figs. 1B, 3B) or to the rate of non-hydrolytic closure of WT CFTR estimated from the closing rate of the K1250R mutant (cf., Fig. 4E, *right, blue bar*). Scheme 3 is a generalization of Scheme 2a in which the $O_1 \rightarrow O_2$ step is allowed to be reversible. Finally, Scheme 4 is a two-component equilibrium model used for fitting the D1370N data in Fig. 1C. Using the notation A⊂B to denote that model A is nested in model B the following relationships hold between the six schemes shown: 1⊂2a⊂2, 1⊂2b⊂2, 2a⊂3, 1⊂4. Importantly, for each of these relationships the distributions of ΔLL values for the case that the submodel is true have been either calculated or empirically determined (26), thereby justifying the use of the log-likelihood ratio test.

Because in a two-open-state model the open-time pdf is decribed by only three parameters (two time constants plus a fractional amplitude), models with more than three free parameters are not identifiable by ML fitting. Not only are such models poorly defined (i.e., an infinite set of parameter vectors yield identical pdfs), but the distributions of ΔLL values are also unknown, precluding interpretation of the obtained log-likelihood ratio in terms of statistical significance. We could therefore not evaluate cyclic models in which more than one step is made reversible at a time. Nor did we include a cyclic model in which step $C \rightarrow O_2$ is made reversible, because (i) we and others have shown that ADP (or ADP+phosphate) does not open CFTR channels, even when applied at high millimolar concentrations (37), and (ii) because in our experiments both ADP and phosphate concentrations were kept at nominally zero levels by a continuously and rapidly flowing ADP- and phosphate-free bath solution.

Fig. S4B summarizes the LL values obtained for fitting the four data sets to each of the schemes in Fig. S4A (relative to the LL value obtained for Scheme 1); and Fig. S4C illustrates the rankings between the models based on the loglikelihood ratio test using P=0.05. These rankings, based solely on the log-likelihood scores, largely confirm our conclusions discussed for the four data sets in the main text. Notably, for all four data sets, Scheme 3 ranked lower than Scheme 2a, suggesting that the ATP-hydrolysis step itself is indeed irreversible, and supporting our choice of Scheme 2 as a framework to interpret our data. Two ranking decisions need further support from independent observations.

For D1370N Schemes 2 and 4 are ranked equal, as both schemes are capable of producing two positive-amplitude exponential components. However, the fit with Scheme 2 yields rate estimates (k_{-1}=0.78 s^{-1}; k_1=4.27 s^{-1}; k_2=0.49 s^{-1}) that are incompatible with the functional interpretation of the steps in Scheme 2 and known consequences of the D-to-N mutation of the Walker-B aspartate in ABC proteins (see main text for references). That is, this fit would suggest a high coupling ratio of 85% with essentially intact ATP hydrolysis, while the mutation is known to abrogate ATP hydrolysis in ABC proteins. Further, based on the extremely slow rate k_2 yielded by this fit, the mutation would have to stabilize the post-hydrolytic NBD dimer by ~100 fold, although it is known to destabilize the dimer due to impaired Mg^{2+} binding. We therefore consider the equilibrium Scheme 4 the best model for describing the gating of D1370N (see discussion in main text).

For partially phosphorylated WT CFTR – but not for fully phosphorylated WT – leaving k_{-1} as a free parameter in Scheme 2 resulted in a small but significant improvement (ΔLL=3.83; P=$6 \cdot 10^{-3}$) relative to fixing it to the rate estimate shown in Fig. 4E (*right, blue bar*). While still predicting a highly non-equilibrium mechanism, the 3-parameter fit (k_{-1}=1.82 s^{-1}; k_1=2.70 s^{-1}; k_2=23.4 s^{-1}) yielded a lower coupling ratio (60%) for partially phosphorylated WT than the one shown in Fig. 4F (95%). However, several independent observations lead us to question the reliability of these rate estimates. First, the large value of 1.82 s^{-1} for rate k_{-1} is inconsistent with the slow closing rate invariably observed for several NBD2 mutants in which ATP hydrolysis is disrupted (K1250A, K1250R, E1371S), or for WT CFTR locked in the open state by non-hydrolyzable ATP analogs (e.g., AMP-PNP). Second, taken at face value, the rankings in Fig. S4C would suggest that k_{-1} for WT increases by ~8 fold upon removal of PKA. While the rapid partial dephosphorylation prevents us from rigorously measuring

closing rates of fully phosphorylated non-hydrolytic mutants (cf., Fig. 2A), there is at least *no evidence* for a major change in this rate upon partial dephosphorylation. E.g., nucleotide removal from K1250R channels opened by 300 nM PKA + 2 mM ATP results in a macroscopic closing rate (0.22±0.004 (n=8)) indistinguishable from the one obtained for channels opened by just 2 mM ATP (0.22±0.01 (n=17)). Third, the ML fitting assumes an ideal, homogeneous data set with rates that remain constant throughout the experiment. Because of the slow gating of CFTR we had to fit pooled data collected from several single-channel patches to obtain sufficient numbers of burst events. E.g., the data for partially phosphorylated WT were pooled from 20 patches. When we subdivided this data into subsets, the improvement by Scheme 2 relative to 2b was not consistently present in all subsets, suggesting data inhomogeneity. To test the effect of such inhomogeneity on the fitting, we simulated 1000 bursts using Scheme 2a with rates k_1=4 s^{-1}, k_2=30 s^{-1}, and 1000 bursts using the same scheme but rates k_1=4 s^{-1}, k_2=50 s^{-1}, and then merged the two data sets. Fitting the pooled data with Scheme 2a resulted in rate estimates k_1=3.92 s^{-1}, k_2=47.6 s^{-1}, together with a large improvement relative to Scheme 1 (ΔLL=21.00; P=$9 \cdot 10^{-11}$). Interestingly, while Scheme 2b fitted only slightly better than 2a (ΔLL=0.51), Scheme 2 fitted significantly better (ΔLL=3.14; P=0.01) yielding rate estimates (k_{-1}=1.83 s^{-1}; k_1=2.32 s^{-1}; k_2=17.3 s^{-1}) similar to those we obtained for fitting our experimental data for partially phosphorylated WT. Taking these limitations into account we consider Scheme 2b as the best approximation of the mechanism of gating of both fully and partially phosphorylated WT CFTR.

Figure legends

Figure S1. Distortion of an essentially single-exponential burst distribution by two alternative burst analysis strategies. *A*, $6x10^6$ events were simulated using the closed (C) - open (O) - blocked (B) scheme (*top left*; rates, in s^{-1}, are printed on the scheme), and the resulting sequence of events (*top right*, *gray* trace illustrates a 20-s segment) subjected to burst analysis using either the method of Jackson et al. ((34); strategy (i)) or that of Magleby and Pallotta ((35); strategy (ii)), to reconstruct two *tentative* sequences of bursts (*center right*, *red* and *blue* traces). As a control, the *true* sequence of bursts (*bottom right*, *black* trace) for this mechanism was obtained by simulating $6x10^6$ events using a gating scheme (*bottom left*) in which the brief (intraburst) closed state B was replaced by a conducting state (O_f), while the rate constants and the seed-value for the random sequence generator remained unchanged. Note 1 interburst closure (*) erroneously eliminated in both reconstructed traces, and 1 intraburst closure (#) mistakenly classified as interburst using strategy (ii). *B*, Open-time histograms constructed from the true sequence (*black*) and the two reconstructed sequences of events (*red*, *blue*), all three normalized to integrate to unity. All three distributions are essentially single-exponential; the *black* and the *blue* traces overlap. *C*, Evaluation of the fractional distortions of the true burst distribution by strategies (i) and (ii). Each bincount of the *red* and *blue* open-time histograms in *B* was divided by the corresponding bincount of the true (*black*) open-time histogram, to yield histograms of fractional distortion (*red* and *blue* histograms in *C*). Because method (ii) equalizes the numbers of misclassified intra- and interburst closures, it causes no distortion to a single-exponential burst distribution. *D*, Estimates of the rate of closing from a burst, obtained by fitting the true sequence (*black* bar) and the two reconstructed sequences of bursts (*red* and *blue* bars) by a C-O scheme using ML. Error bars are 0.5-unit log-likelihood intervals, but are too small to be seen. Method (ii) returns an unbiased estimate.

Figure S2. Distortion of the burst distribution of a cyclic mechanism by two alternative burst analysis strategies. *A*, $7x10^6$ events were simulated using a cyclic mechanism (*top left*; rates are printed on the scheme) like Scheme 2 with $k_{-1}=0$ (Fig. 1A), supplemented with brief intraburst closed states (C_{f1}, C_{f2}). (For the purpose of studying open bursts, the two closed states C_1 and C_2 in Scheme 2

are merged here into a single state C.) The resulting sequence of events (*top right*, *gray* trace illustrates a 20-s segment) was subjected to burst analysis using either strategy (i) or (ii) (see Methods), to reconstruct two *tentative* sequences of bursts (*center right*, *red* and *blue* traces). As a control, the *true* sequence of bursts (*bottom right*, *black* trace) for this mechanism was obtained by simulating $7x10^6$ events using a gating scheme (*bottom left*) in which the brief (intraburst) closed states C_{f1} and C_{f2} were replaced by conducting states (O_{f1}, O_{f2}), while the rate constants and the seed-value for the random sequence generator remained unchanged. Note 2 intraburst closures (#) erroneously misclassified as interburst using strategy (ii), the second of them also misclassified using strategy (i). *B*, Open-time histograms constructed from the true sequence (*black*) and the two reconstructed sequences of events (*red*, *blue*), all normalized to integrate to unity. *C*, Evaluation of the fractional distortions of the true burst distribution by strategies (i) and (ii). Each bincount of the *red* and *blue* open-time histograms in *B* was divided by the corresponding bincount of the true (*black*) open-time histogram, to yield histograms of fractional distortion (*red* and *blue* histograms in *C*). *D*, Estimates of the rates $O_1 \rightarrow O_2$ (*left*) and $O_2 \rightarrow C$ (*right*), obtained by fitting the true sequence (*black* bars) and the two reconstructed sequences of bursts (*red* and *blue* bars) by Scheme 2 with k_{-1} fixed to zero, using ML. Barely visible error bars are 0.5-unit log-likelihood intervals. Note that, overall, method (i) causes less distortion (*C*) and provides more accurate rate estimates (*D*) for this mechanism.

Figure S3. Defining ATP-dependent bursts for WT and D1370N CFTR. *A*, Current trace from a single pre-phosphorylated WT CFTR channel gating at steady state in 2 mM ATP (*left*) and macroscopic current response (*right*) of >100 pre-phosphorylated WT CFTR channels to a brief exposure (*bar*) to 2 mM ATP. The *red line* is a single-exponential fit to the current decay time course following ATP removal, yielding a time constant of 259 ms. *B*, Closed-time histogram pooled from two single-channel records including the one shown in *A*. The *red line* is a ML fit by a mixture of 2 exponentials; individual components are depicted by *dashed lines*, and time constants are indicated. (The third long component with vanishing fractional amplitude apparent in the histogram was not typically observed.) The *blue line* depicts t_{crit} using strategy (i) and assuming 1 intra- and 1 interburst component. Using this t_{crit}, burst analysis of this set of data yielded a mean burst duration of 278 ms. *C*,

Current trace from a single pre-phosphorylated D1370N CFTR channel gating at steady state in 2 mM ATP. *D*, Closed-time histogram pooled from four single-channel records including the one shown in *C*. The *red line* is a ML fit by a mixture of 4 exponentials; individual components are depicted by *dashed lines*, and time constants are indicated. Burst analysis (using strategy (ii)) based on assigning 1, 2, or 3 components as intraburst yielded mean burst durations of 518 ms, 1324 ms, and 12.4 s, respectively; the *blue line* depicts t_{crit} using strategy (ii) and assuming 2 intraburst components. *E*, Macroscopic current response of ~100 pre-phosphorylated D1370N CFTR channels to a brief exposure (*bar*) to 2 mM ATP. The *red line* is a single-exponential fit to the current decay time course following ATP removal, yielding a time constant τ=1.32 s; average τ was 1.4±0.1 s (n=3). Asterisks mark infrequent brief spontaneous openings in the absence of ATP. *F*, Dwell-time histogram of intraburst closures collected from stretches of record in which only one D1370N channel has remained in the bursting state following ATP removal (see inset in *E*, period marked by *blue bar*). Closed events before the final closure (these must be intraburst given the lack of ATP in the bath) were pooled from 34 experiments. The *red line* is a ML fit by a mixture of 2 exponentials; individual components are depicted by *dashed lines*, and time constants are indicated. Note, that these time constants are similar to those of the two briefest components of the steady-state closed-time distribution (Fig. S3D).

Fig. S4. Comprehensive summary of ML fitting results. *A*, Two linear, equilibrium, and four cyclic, non-equilibrium, models were tested for their ability to describe the distributions of burst durations. Free parameters are shown in *red*. *B*, Summary of log-likelihood (LL) values obtained for fitting the six schemes in *A* to the distributions of burst durations of fully phosphorylated WT, and of partially phosphorylated WT, K464A, and D1370N CFTR channels. LL values are presented relative to that obtained for fitting the same data set with Scheme 1 (i.e., for Scheme *n*, LL(*n*)-LL(1) is shown). *C*, Rankings of the six schemes in *A* for each of the four data sets, obtained using the log-likeliohood ratio test with P=0.05. The highest ranked model appears on the right.

Fig. S1

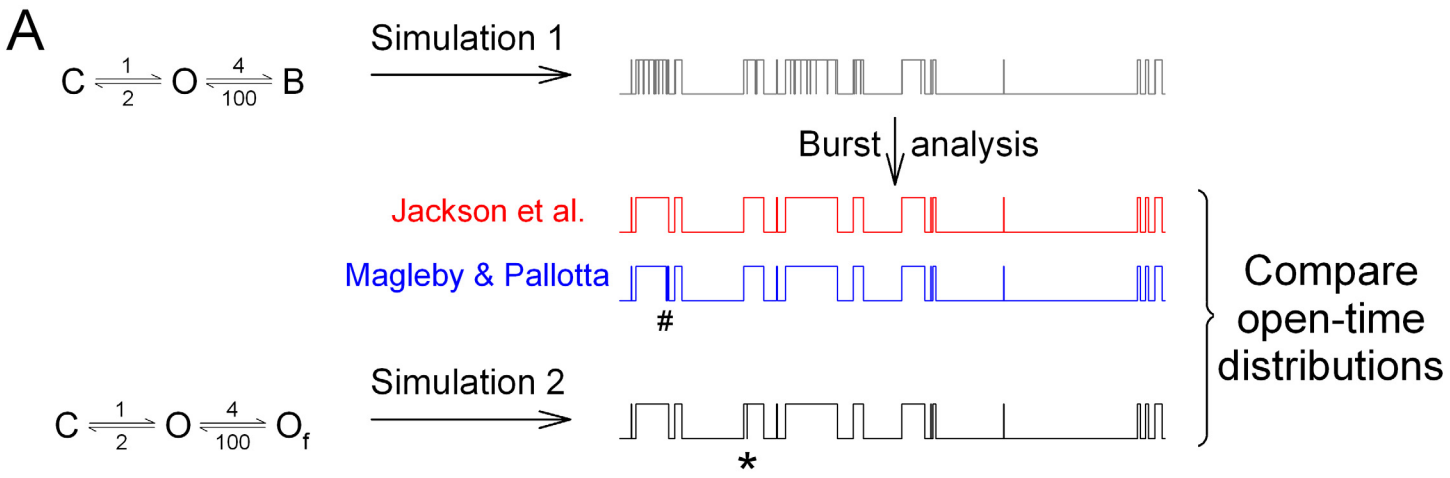
A
C 1/2 O 4/100 B
Simulation 1
Burst analysis
Jackson et al.
Magleby & Pallotta
#
Simulation 2
C 1/2 O 4/100 O_f
*
Compare open-time distributions

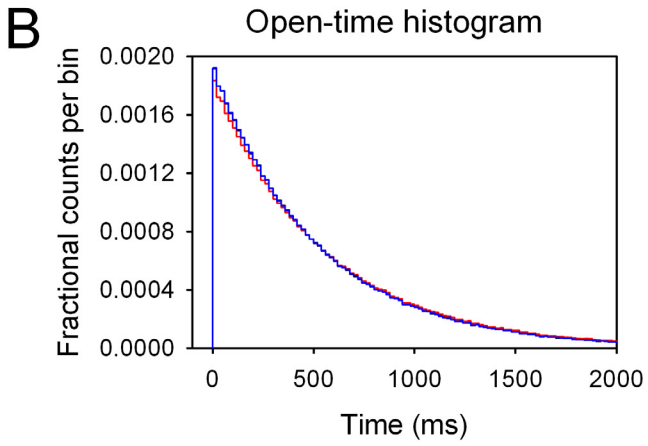
B
Open-time histogram
Fractional counts per bin
0.0020
0.0016
0.0012
0.0008
0.0004
0.0000
0
500
1000
1500
2000
Time (ms)

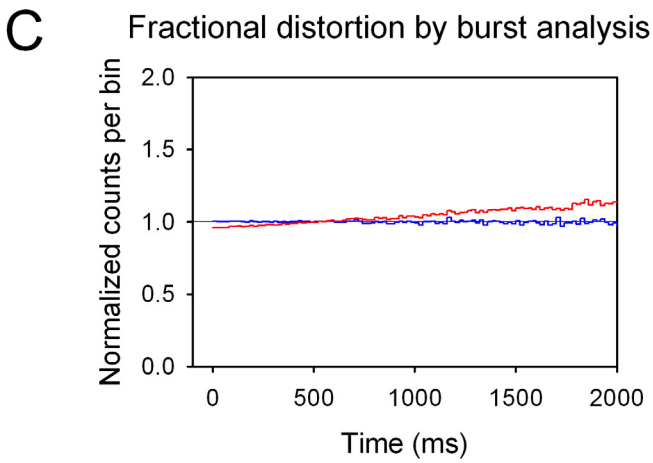
C
Fractional distortion by burst analysis
Normalized counts per bin
2.0
1.5
1.0
0.5
0.0
0
500
1000
1500
2000
Time (ms)

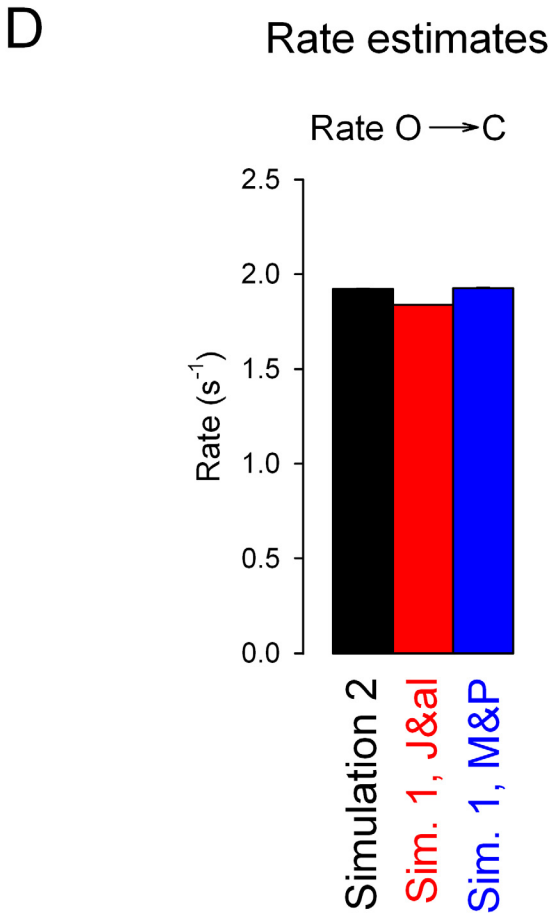
D
Rate estimates
Rate O → C
Rate (s^-1)
2.5
2.0
1.5
1.0
0.5
0.0
Simulation 2
Sim. 1, J&al
Sim. 1, M&P

Fig. S2

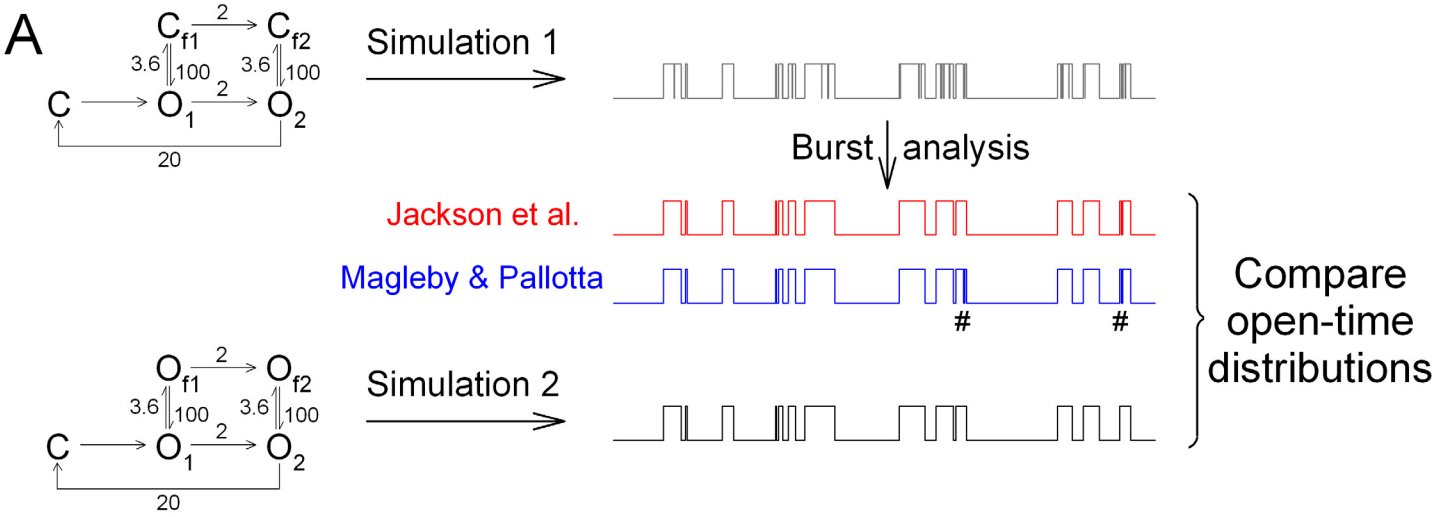
A
C
O1
O2
Cf1
Cf2
Of1
Of2
2
3.6
100
20
Simulation 1
Simulation 2
Burst analysis
Jackson et al.
Magleby & Pallotta
#
Compare open-time distributions

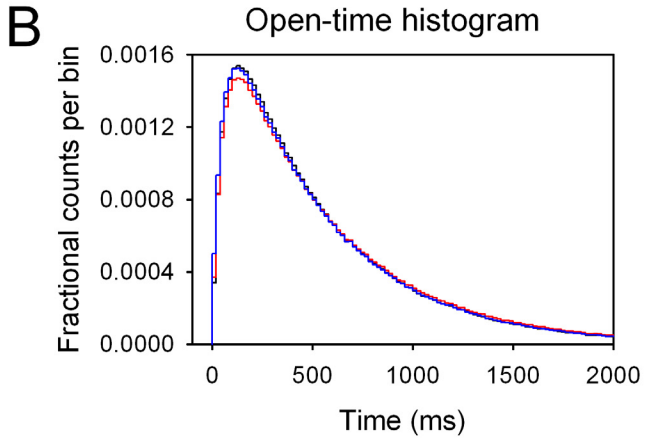
B
Open-time histogram
Fractional counts per bin
0.0016
0.0012
0.0008
0.0004
0.0000
0
500
1000
1500
2000
Time (ms)

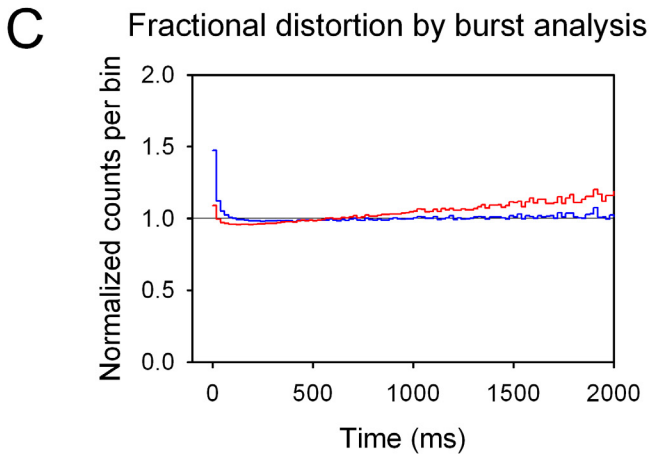
C
Fractional distortion by burst analysis
Normalized counts per bin
2.0
1.5
1.0
0.5
0.0
0
500
1000
1500
2000
Time (ms)

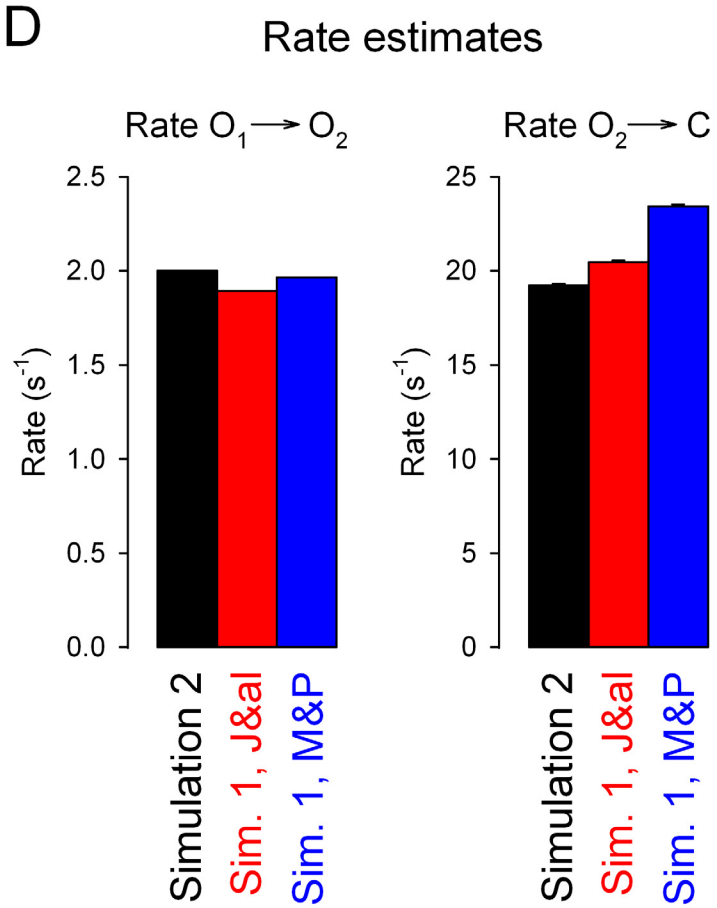
D
Rate estimates
Rate O1 → O2
Rate O2 → C
Rate (s-1)
2.5
2.0
1.5
1.0
0.5
0.0
25
20
15
10
5
0
Simulation 2
Sim. 1, J&al
Sim. 1, M&P

Fig. S3

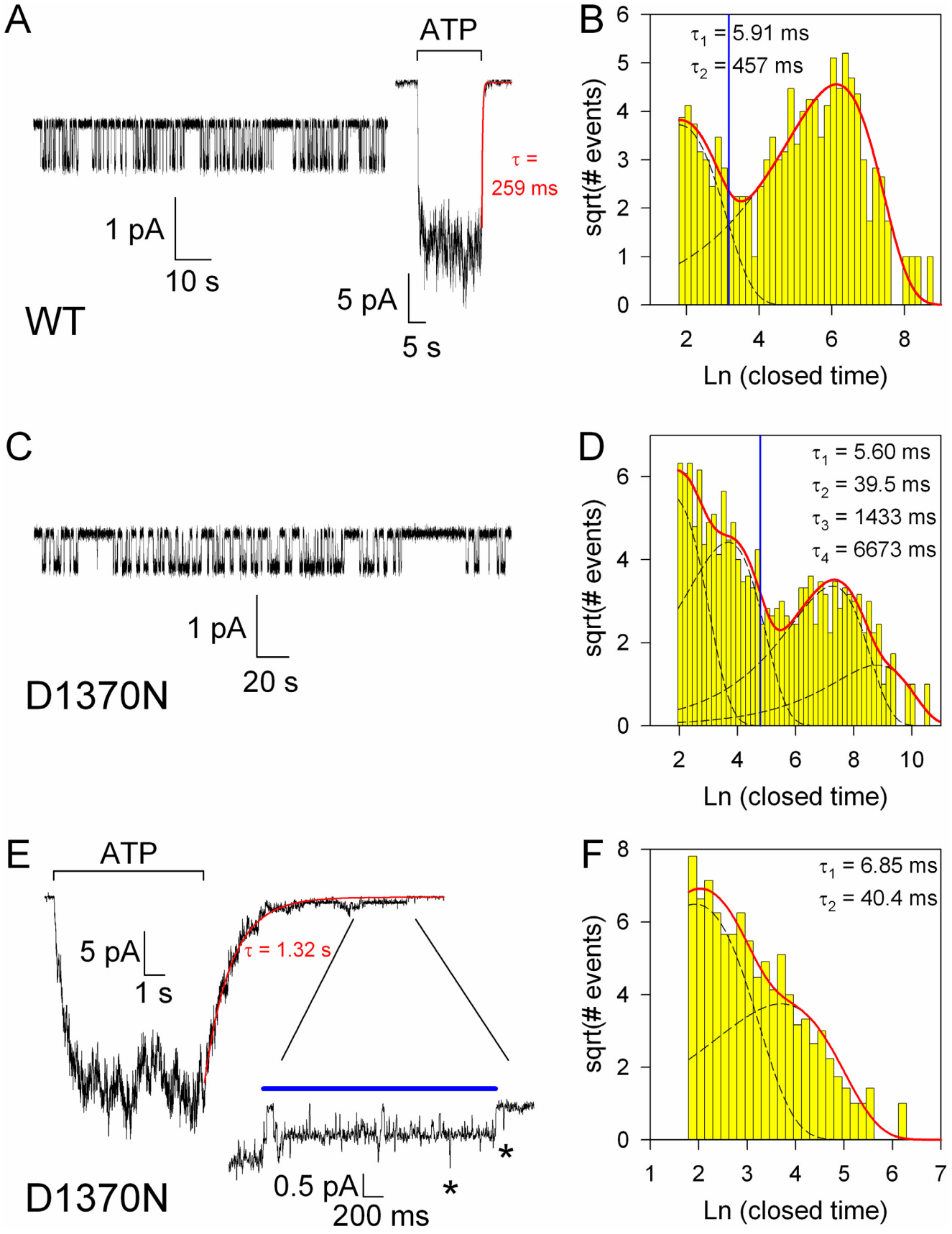
A
ATP
τ = 259 ms
1 pA
10 s
5 pA
5 s
WT
B
τ1 = 5.91 ms
τ2 = 457 ms
sqrt(# events)
Ln (closed time)
C
1 pA
20 s
D1370N
D
τ1 = 5.60 ms
τ2 = 39.5 ms
τ3 = 1433 ms
τ4 = 6673 ms
sqrt(# events)
Ln (closed time)
E
ATP
5 pA
1 s
τ = 1.32 s
0.5 pA
200 ms
D1370N
F
τ1 = 6.85 ms
τ2 = 40.4 ms
sqrt(# events)
Ln (closed time)

Fig. S4

A

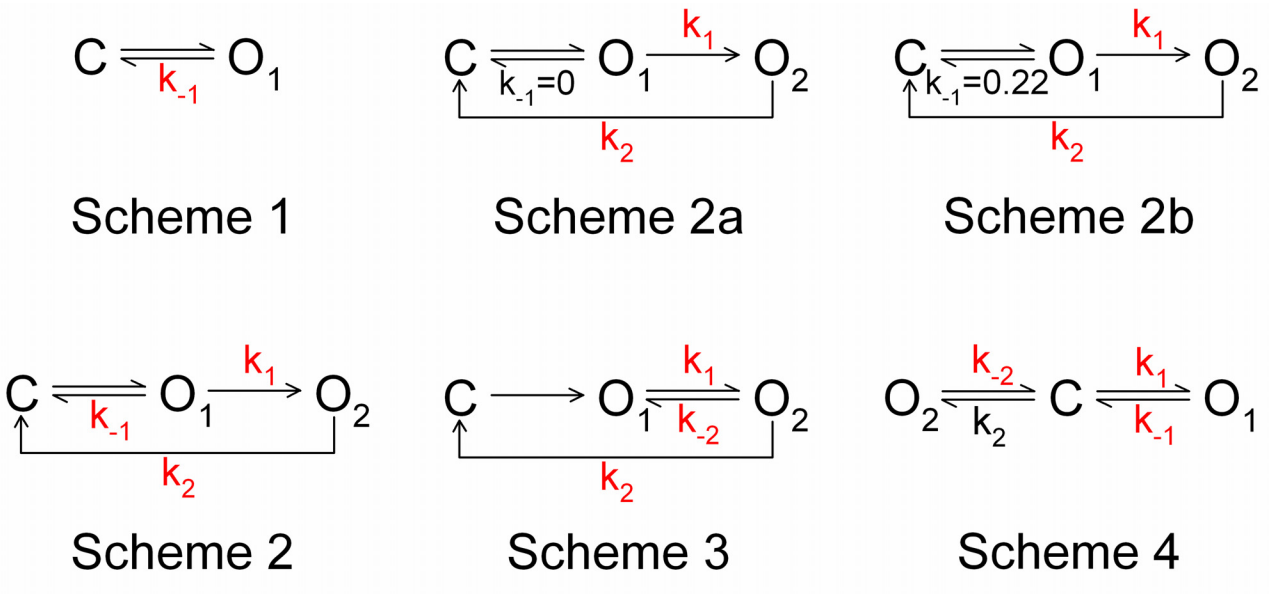

B

	Sch. 4	Sch. 1	Sch. 2a	Sch. 3	Sch. 2b	Sch. 2
WT+PKA	0.00	0	17.34	17.34	19.03	20.26
WT	0.00	0	18.01	18.01	18.83	22.66
K464A	0.00	0	0.00	0.00	0.00	3.62
D1370N	3.24	0	0.00	0.00	0.00	3.24

C

WT+PKA: Sch. 4 < Sch. 1 << Sch. 3 < Sch. 2a < Sch. 2 < Sch. 2b

WT: Sch. 4 < Sch. 1 << Sch. 3 < Sch. 2a < Sch. 2b < Sch. 2

K464A: Sch. 4 < Sch. 3 < Sch. 2a = Sch 2b < Sch. 1 < Sch. 2

D1370N: Sch. 3 < Sch. 2a = Sch 2b < Sch. 1 < Sch. 2 = Sch. 4